論文 / 著書情報
Article / Book Information

Title	Thermal diffusivity and conductivity of sulfide and oxide solid electrolytes: Effects of densification and microstructural evolution
Authors	Hayoung Lee, Yuto Seki, Atsuro Okumura, Manabu Kodama
Citation	Journal of Energy Storage, Vol. 145, , p. 119926
Pub. date	2026, 2
DOI	https://dx.doi.org/10.1016/j.est.2025.119926
Creative Commons	Information is in the article.

Journal of Energy Storage 145 (2026) 119926

Contents lists available at ScienceDirect

Journal of Energy Storage

journal homepage: www.elsevier.com/locate/est

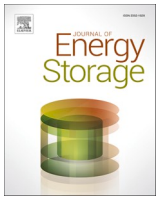

Research papers

Thermal diffusivity and conductivity of sulfide and oxide solid electrolytes: Effects of densification and microstructural evolution

Hayoung Lee [a], Yuto Seki [a], Atsuro Okumura [a], Manabu Kodama [a,*]

[a] Institute of Science Tokyo, 2-12-1 Oookayama, Meguro-ku, Tokyo, 152-8550, Japan

ARTICLE INFO

Keywords:
Solid electrolyte
Thermal conductivity
Thermal diffusivity
Ionic conductivity
Volume fraction
Tortuosity

ABSTRACT

Solid electrolytes (SEs), essential for all-solid-state batteries, exhibit high thermal resistance and can reduce the cooling system requirements. However, limited cooling under high-rate charging and discharging can cause thermal issues, constraining battery performance. To address these challenges, it is important to clarify the thermal transport characteristics of SEs, which remain underexplored. In sulfide SEs, structure varies with molding pressure during fabrication, while in oxide SEs, it changes with sintering temperature. This study investigates how such structural changes affect the thermal transport properties of three sulfide SEs (LPS glass, Li_3PS_4 glass ceramic and Li_6PS_5Cl) and an oxide SE ($Li_{6.25}Ga_{0.25}La_3Zr_2O_{12}$). For sulfide SE, thermal transport characteristics were also compared with ionic conductivity. Structural analyses confirmed that increasing molding pressure or sintering temperature enhanced particle integration and densification. Thermal conductivity increased significantly with densification due to improved transport pathways and reduced tortuosity, consistent with trends in ionic conductivity. In contrast, thermal diffusivity increased only slightly, as higher density raised both thermal conductivity and volumetric heat capacity, the latter suppressing thermal diffusivity.

1. Introduction

Lithium-ion batteries are currently used in electric vehicles and offer numerous advantages, including high energy density and a long life cycle [1]. However, conventional lithium-ion batteries rely on organic liquid electrolytes, which are flammable and exhibit low thermal stability, leading to concerns about fire and bursting risks [2,3]. Hence, all-solid-state lithium-ion batteries (ASSLiBs), which replace the organic liquid electrolyte and separator with an inorganic solid electrolyte (SE), are gaining attention as promising candidates for next-generation rechargeable batteries in electric vehicles [4]. The operating principle of ASSLiBs is fundamentally the same as that of conventional liquid-based batteries. During charging, lithium ions are released from the cathode active materials and migrate to the anode active materials through the SE, while electrons flow through an external circuit in the same direction. During discharging, this process is reversed, with lithium ions and electrons moving back to the cathode active materials [5]. Although the basic operating mechanism is similar, the SE provides enhanced heat resistance and flame-retardant characteristics, reducing the need for cooling systems and enabling the installation of more battery cells within the same battery pack volume, thereby increasing the effective energy density [6].

However, thermal conduction and natural convection under minimized cooling conditions generally support inherently slow heat transfer, leading to potential thermal issues, despite the high thermal stability of the SE. One notable issue involves the degradation of both the SE and the active material owing to interfacial reactions, which are accelerated at elevated temperatures [7]. When the heat transfer within the battery is slow, local temperatures rise with the increased heat generation, promoting SE–active material reactions [8]. This may reduce the ionic conductivity of the SE and the capacity of the active material, ultimately degrading the overall battery performance. Furthermore, slow heat transfer can cause non-uniform temperature distributions within the battery pack [9]. Given that the internal resistance of a battery decreases at higher temperatures and increases at lower temperatures, this non-uniformity results in uneven charge/discharge behavior among batteries, thereby reducing the apparent battery capacity. To address the thermal issues associated with the slow heat transfer and improve the effective energy density of battery packs by reducing the need for a cooling system, a precise thermal design of the entire battery pack is essential. This requires a comprehensive understanding of the factors affecting heat transfer within battery materials, especially the SEs,

* Corresponding author.
E-mail address: kodama.m.d0f2@m.isct.ac.jp (M. Kodama).

https://doi.org/10.1016/j.est.2025.119926
Received 4 June 2025; Received in revised form 4 November 2025; Accepted 13 December 2025
Available online 20 December 2025

which play a critical role in the thermal management of ASSLiBs.

Despite the importance of proper thermal design for high-performance ASSLiBs, most research on SEs in ASSLiBs has primarily focused on improving electrochemical performance, including enhancements in ionic conductivity and electrochemical stability [10–14]. Only a few studies have analyzed the thermal transport characteristics of SEs [15,16]. Cui et al. analyzed the thermal conductivity of oxide SEs, namely $Li_{1.70}Al_{0.61}Ge_{1.35}$, $P_{3.04}O_{12.0}$, and $Li_{1.31}Al_{0.42}Ge_{1.52}P_{3.09}O_{12.1}$, revealing that variations in porosity, induced by changes in the sintering temperature and duration, significantly influenced thermal conductivity [15]. Cheng et al. reported that oxide SEs, such as $Li_{6.4}La_3Zr_{1.4}Ta_{0.6}O_{12}$ and $Li_{1.5}Al_{0.5}Ge_{1.5}P_3O_{12}$, exhibit higher thermal conductivity and thermal stability than sulfide SEs. For example, Li_6PS_5Cl, and Na_3PS_4 have relatively low thermal conductivities [16]. These studies provide valuable insights into the thermal conductivity of oxide and sulfide SEs, but the effects of the microstructural changes introduced during fabrication on thermal conductivity remain insufficiently explored, particularly for sulfide SEs. Furthermore, the thermal issues caused by slow heat transfer must be considered, necessitating not only an understanding of the thermal conductivity, but also an evaluation of the temperature distribution under operating conditions. In this context, the thermal diffusivity, a key transport parameter explicitly used in the heat conduction equation to describe temperature gradients, also requires further investigation. During the synthesis and preparation of battery materials, significant microstructural changes can occur, such as variations in the volume fraction and tortuosity. For instance, in sulfide SEs, the microscale structure undergoes modifications depending on the molding pressure, and in oxide SEs, the structure depends on the sintering temperature [17–19]. Microstructural variations are expected to impact the thermal transport characteristics. Therefore, this study focuses on elucidating the influence of these structural changes on the thermal transport characteristics of SEs.

Considering their microstructure, the thermal transport characteristics of SEs can be interpreted based on the characteristics of porous materials. Maxwell and Bruggeman proposed theoretical models to predict the effective thermal conductivity of porous materials based on parameters such as porosity and pore size [20,21]. These approaches have been experimentally and numerically confirmed and applied to a wide range of porous materials [22–24]. Moreover, Kerrisk reported a mathematical model describing the effective thermal diffusivity and thermal conductivity of porous materials [25], but experimental studies remain limited in the case of thermal diffusivity. Additionally, these models can vary in their applicability, depending on the material properties of the porous media. Therefore, experimental investigations focused on SEs are required.

In this study, we investigated the effects of structural changes in SEs, induced by varying the molding pressure for sulfide SEs and sintering temperature for oxide SE, on their thermal transport characteristics, namely the thermal conductivity and thermal diffusivity. Three sulfide SEs, including LPS glass with a Li_2S:P_2S_5 = 75:25 composition, Li_3PS_4 glass ceramic (LPS glass ceramic), and Li_6PS_5Cl and one oxide SE, $Li_{6.25}Ga_{0.25}La_3Zr_2O_{12}$, were evaluated herein. For sulfide SEs, the thermal transport characteristics are also compared with the ionic conductivity, a representative transport parameter in batteries, to gain further insights into the overall transport behavior. This work elucidates the effects of structural changes on thermal transport in SEs and supports the optimal preparation of SE materials for high-performance ASSLiBs.

2. Experimental procedures

Herein, experimental studies were conducted using sulfide SEs (LPS glass [26], LPS glass ceramic [27], and Li_6PS_5Cl [28]) and an oxide SE ($Li_{6.25}Ga_{0.25}La_3Zr_2O_{12}$ [29]). All SEs were synthesized via solid-state reactions, as described below. The internal microstructure of sulfide SEs was analyzed by X-ray computed tomography (X-ray CT; nano3DX, Rigaku), and the fracture surfaces of oxide SE were analyzed by scanning electron microscopy (SEM; TM-4000, Hitachi). Fracture toughness of the sulfide SEs was evaluated by Vickers indentation method (Mitutoyo, HM-201C). Ionic conductivity of sulfide SE was measured by electrochemical impedance spectroscopy (EIS; Squidstat Plus, Admiral Instruments). Thermal diffusivity was measured using a measurement system that employs the thermal wave method (Mobile M3 type 1, ai-Phase Co., Ltd.), which minimizes both the material degradation and the influence of thermal contact resistance. The thermal conductivity is calculated based on the measurements of the thermal diffusivity and volume fraction of SEs. All experiments of sulfide SE were conducted in a low-humidity (< −80 °C) argon-filled glove box, considering that sulfide SEs react with moisture in the air to produce toxic hydrogen sulfide gas.

2.1. Fabrication of the SEs

All sulfide SE samples were obtained via solid-state reactions. Specifically, 3 g of LPS glass [26] was synthesized using a mechanical milling process without any subsequent heat treatment. The starting materials, Li_2S and P_2S_5 powders, were placed in a 50 ml zirconia pot with 16 zirconia balls (10 mm diameter) and 0.2 ml of diethyl ether as a grinding aid. Mechanical milling was conducted using a high-energy vibration mill (Emax, Retsch), operating at 1200 rpm for 10 h. Then, 3 g of LPS glass ceramic [27], which exhibits a higher degree of crystallinity than amorphous LPS glass, was obtained by heat-treating the synthesized LPS glass at 300 °C for 10 h. Similarly, 3 g of Li_6PS_5Cl [28], which possesses the most pronounced crystalline characteristics among the three, was synthesized by mechanically milling Li_2S, P_2S_5, and LiCl powders at 1200 rpm for 10 h, followed by calcination at 470 °C for 10 h. Samples were compressed using pressures of 15, 50, 100, and 200 MPa.

Oxide SEs were also synthesized via solid-state reactions. Herein, 3 g of $Li_{6.25}Ga_{0.25}La_3Zr_2O_{12}$ [29] was obtained using La_2O_3, ZrO_2, Ga_2O_3, and LiOH powders. The starting materials were placed in a 50 ml zirconia pot for planetary ball milling (LP-M2, Ito Seisakusho Co., Ltd.), along with 20 zirconia balls (10 balls with a 10 mm diameter and 10 balls with a 5 mm diameter) and 25 ml of hexane. Planetary ball milling was conducted at 300 rpm for 2 h. After milling, the ground materials were transferred to a platinum crucible and subjected to calcination for pre-sintering in an electric furnace (CWF13/5, Carbolite Gero) at 800 °C for 12 h, with a temperature increase rate of 5 °C/min. Then, a second ball milling step was performed under the same conditions, followed by pellet formation under 150 MPa. The pellets were then placed into a platinum crucible, covered with mother powders, and subjected to calcination for sintering at the specified temperatures for 12 h, with a temperature increase rate of 5 °C/min and a temperature decrease rate of 2 °C/min. Samples were sintered during the main calcination step at 800, 950, 1050, 1100, and 1150 °C. Finally, the fabricated $Li_{6.25}Ga_{0.25}La_3Zr_2O_{12}$ samples were shaved using #1500 sandpaper.

Once the fabrication of SEs is completed, an X-Ray Diffraction (XRD) experiment, which is the basic technique for obtaining information on the atomic structure of crystalline solids, was performed as an evaluation of the SEs. XRD patterns were acquired using a Rigaku Miniflex (Rigaku Corporation, Japan) with a Cu-Kα source in the 2θ/θ range of 10°-60°. Fig. 1 shows the XRD patterns of SEs powder. It is very similar to those of previous study, so it can be confirmed that SEs was fabricated well [17,26–30].

2.2. Structural analysis

2.2.1. Observation of the structural changes and calculation of the structural parameters

For sulfide SE samples, the X-ray CT jig containing the SE powders compressed at each molding pressure was mounted onto the X-ray CT system. By rotating the jig stage, structural changes of the sulfide SEs can be observed from various directions. The X-ray CT jig used in this study is almost identical to that reported in a previous study [17]. X-ray CT measurements were performed using a quasi-parallel optics X-ray CT

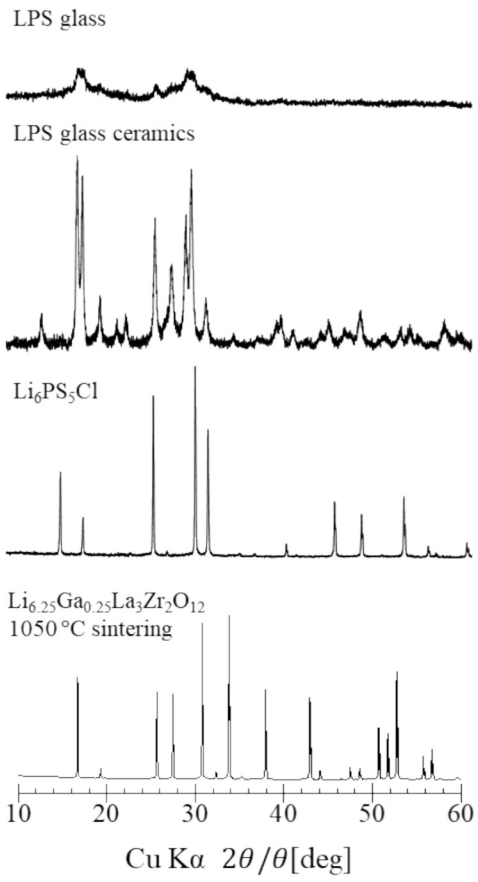

Fig. 1. XRD patterns of sulfide and oxide SEs (LPS glass, LPS glass ceramics, Li_6PS_5Cl and $Li_{6.25}Ga_{0.25}La_3Zr_2O_{12}$).

system. The CT images of the sample were binarized into pore and solid regions using a global thresholding method, where a single threshold value was applied to the entire image. The threshold for binarization was determined based on the contrast between the dark and bright regions in the CT images. Voxels with values below the threshold were classified as pores, and those above the threshold were classified as the SE. An example of binarized image is shown in Fig. S1. The binarized images were then stacked to reconstruct the 3D structure of the SEs, and the volume fraction was determined from the number of voxels corresponding to the SE region. The final volume fraction value was obtained by averaging the results from the three independent measurements. The measurement variability was within 3.4 %. The result of volume fraction was validated by comparison with the relative density calculated from the pellet density, confirming the reliability of the binarization approach. The tortuosity of the sulfide SEs was evaluated by performing an electric field analysis on the reconstructed 3D structures, following previously reported procedures [17,31]. The distributions of electric potential and ion current density were obtained by solving the governing Eqs. (1), (2), (3), (4) with the finite-volume method.

$$\nabla \times \vec{E} = 0 \tag{1}$$

$$\vec{E} = -grad\varphi \tag{2}$$

$$\nabla \bullet \vec{j} = 0 \tag{3}$$

$$\vec{E} = \sigma \bullet \vec{j} \tag{4}$$

Here, $\vec{E}$ is the electrical field vector, φ is electrical potential, $\vec{j}$ is the current density vector, σ is the ionic conductivity. Based on the resulting distributions of electric potential and ion current density, the effective ionic conductivity was evaluated, and the tortuosity of the solid electrolyte was determined. As boundary conditions, a potential difference of 1 V was applied between the top and bottom surfaces of the reconstructed 3D structure, and the ionic conductivity of pores other than the SE was set to zero. The voxel size of the reconstructed X-ray CT images was approximately 0.52 μm, and the analyzed domain size for volume fraction and tortuosity calculation was $700 \times 700 \times 700$ voxels. To enable clear observation of the structural changes due to molding pressure in CT images, 75–150 μm particles were used because such changes are less discernible in smaller particles.

In order to properly discuss the actual microstructural changes of SEs under different fabrication parameters, it is important to observe their internal particle structures, for which X-ray CT is the suitable method. However, for oxide SE samples, because their X-ray absorption is higher than that of sulfide SEs, clear CT images cannot be obtained owing to insufficient transmission of the X-rays to the detector. Although advanced 3D imaging techniques such as focused ion beam (FIB) tomography can provide high-resolution 3D visualization, FIB tomography is a destructive method that involves sequential ion milling of the sample surface and has a limited observable area. Therefore, in this study, the porosity and morphology of oxide SEs were characterized using 2D SEM observations of the fracture surfaces and pellet density measurements, which offer sufficient spatial resolution and a wide observable region without damaging the sample. The fracture surfaces of the $Li_{6.25}Ga_{0.25}La_3Zr_2O_{12}$ pellets sintered at different temperatures were observed by SEM, where the pellet surface was irradiated with an electron beam and the reflected electrons were detected to visualize the detailed surface morphology beyond the resolution of optical microscopes. To quantitatively evaluate the structure, the volume fraction of $Li_{6.25}Ga_{0.25}La_3Zr_2O_{12}$ sintered at each temperature was determined by dividing the measured pellet density by its theoretical density.

2.2.2. *Vickers indentation fracture toughness test*

The fracture toughness of the sulfide SEs was evaluated using the Vickers indentation fracture toughness test, following a previously reported method [30]. Briefly, a Vickers hardness tester (Mitutoyo, HM-201C) was used to create indentations, and SEM was employed for surface observation. The Vickers hardness tester was installed inside a glove box to prevent reactions with moisture in the air. The fracture toughness was measured by first pressing the Vickers indenter into the sample surface at an applied load of 0.5 kgf to create indentations. The indentation lengths and crack sizes were then measured for calculation.

$$K_C = 0.026\left(E^{\frac{1}{2}}P^{\frac{1}{2}}a \Big/ c^{\frac{3}{2}}\right) \tag{5}$$

Here, K_C is the fracture toughness, E is the Young's modulus, P is the applied load, c is the average half-crack length, and a is the average half-diagonal length of the indentation. A representative value for the Young's modulus of each sulfide SE was used [16]. In the Vickers indentation fracture toughness test, the indentation is affected by the presence of pores within the pellet, since the applied load can contribute to the reduction of internal porosity. To minimize this effect and ensure more reliable measurements, pellets were prepared by pressing the powders under the highest molding pressure used in this study, 200 MPa, for 4 min. As will be described later, at this pressure, the sulfide SEs exhibited the lowest porosity and sufficient densification, resulting in comparable porosity levels among different sulfide SEs. Furthermore, in the case of sulfide SEs with larger particle sizes, the presence of large interparticle pores makes crack evaluation difficult. To minimize this issue, sulfide SE powders with particle sizes below 40 μm were used. To accurately measure the fracture toughness of the sulfide SEs, pellets with sufficient thickness were also required [32]. Therefore, 50 mg of each powder was used. As a result, the pellets were then prepared by pressing the powders under a molding pressure of 200 MPa for 4 min.

Furthermore, eight indentations were made on each sulfide SE pellet, ensuring that the distance between adjacent indentations was greater than 4*c* [33]. The final fracture toughness value was obtained by averaging the results from the eight measurements.

2.3. Measurements of the thermal and ionic transport characteristics

Thermal diffusivity was measured using the thermal wave method, which minimizes the contact resistance between the sample and the device, as well as the material degradation by leveraging very small temperature fluctuations. In the thermal wave method, a sinusoidal thermal input is applied to the pellet, and the resulting temperature oscillations are measured. As the thermal wave propagates through the pellet, its amplitude attenuates and its phase shifts because of thermal diffusion [34,35]. The pellet was placed between the heater and the sensor, and by measuring the phase delay and knowing the pellet thickness, the thermal diffusivities of the pellets fabricated under different molding pressures and sintering temperatures were determined. The average thermal diffusivity of each pellet was calculated using the four measurements. The measurement variability was within 3.9 % for the sulfide SEs and 1.7 % for the oxide SE. For sulfide SEs, to avoid an increase in apparent thermal diffusivity caused by the thermal diffusivity of argon gas trapped in the gap between the pellet and the heater or sensor due to poor contact, pellets were fabricated from 25 mg of powder, which was determined to be the most appropriate amount, within the measurable range of the measurement device. In addition, because 75–150 μm particles were used for observing structural changes via X-ray CT, it was necessary to evaluate the corresponding thermal diffusivity under the same conditions. Therefore, the thermal diffusivity was measured using pellets composed of particles within the same size range (75–150 μm).

The thermal conductivity of the SEs under various molding pressures and sintering temperatures was calculated from four independent measurements of thermal diffusivity, along with the corrected density and specific heat. The measurement variability was within 4.5 % for the sulfide SEs and 2.0 % for the oxide SE. The corrections for density and specific heat were based on a mathematical model developed for the thermal conductivity of heterogeneous and porous materials [25]. The theoretical specific heat and theoretical density of SEs required to obtain the corrected density and specific heat were determined from reference values [16,36,37].

Regarding ionic conductivity, the X-ray CT jig containing the SE powders compressed at each molding pressure was connected to the potentiogalvanostat EIS system. Impedance measurements were performed over a frequency range from 1 MHz to 100 Hz to obtain Nyquist plots, and the plots were analyzed to determine the bulk resistance and calculate ionic conductivity.

3. Results and discussion

3.1. Structural analysis of the sulfide SEs

Fig. 2 shows the influence of the molding pressure on the structure of all three sulfide SE (LPS glass, LPS glass ceramic, and Li_6PS_5Cl), as observed by X-ray CT. The white regions represent sulfide SE particles, and the black regions represent pores. For the LPS glass prepared at a low molding pressure (15 MPa), partial fracture had already produced particles smaller than the initial 75–150 μm size range, while the overall particle morphology remained distinguishable. With increasing molding pressure, such fracture became more pronounced, and the resulting small SE particles filled in the pores. Moreover, the particles become more integrated, and the porosity decreases, consistent with previous studies [17,19]. In the study by Perrenot et al., molding pressure and pressing time were identified as the key parameters governing the porosity of sulfide SEs. Among them, porosity was reported to be predominantly influenced by molding pressure, while the effect of pressing time was comparatively minor [38]. Table 1 summarizes the average volume fractions of sulfide SEs as a function of processing conditions, including molding pressure, pressing time, and particle size distribution. In this study, X-ray CT measurements were performed using a jig configuration in which the molding pressure was continuously maintained, and all sulfide SEs were prepared with the same particle size distribution. The results showed that densification occurred irrespective of the pressing time. This suggests that, since the pressing duration in our experiments always exceeded the minimum threshold of 10 min reported by Perrenot et al., the structural changes induced by

Table 1
Summary of volume fractions in sulfide SEs under various processing conditions.

Molding pressure [MPa]	15	50	100	200
Pressing time	Maintain pressure (over 10 min)			
Particle size distribution [μm]	75–150			
LPS glass Volume fraction [%]	52.4	65.8	73.0	77.7
LPS glass ceramics Volume fraction [%]	57.8	65.1	73.1	77.5
Li_6PS_5Cl Volume fraction [%]	62.5	68.3	73.8	76.9

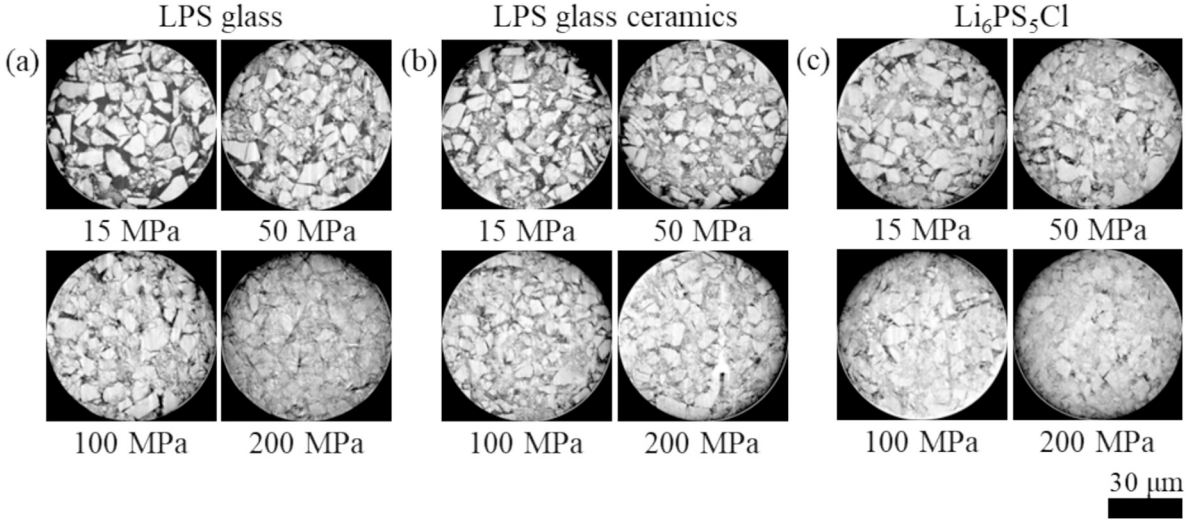

Fig. 2. X-Ray CT images of the structural changes in (a) LPS glass, (b) LPS glass ceramic, and (c) Li_6PS_5Cl prepared using molding pressures of 15, 50, 100, and 200 MPa.

compaction had already converged under our conditions. This behavior is attributed to the room-temperature pressure sintering capability of sulfide SEs [17]. Given the low covalent bonding energy between Li and S, local ion diffusion occurs at particle boundaries under sufficiently high molding pressures, even at room temperature. This ion mobility contributes to the blurring of the interparticle boundaries and the elimination of pores, thereby promoting densification even without additional thermal treatment. Furthermore, their relatively low Young's modulus compared with oxide SEs enables more uniform stress distribution during pressing, which facilitates particle contact, enhances interparticle bonding, and ultimately promotes densification [19]. Moreover, both the LPS glass ceramic and Li_6PS_5Cl exhibit increased densification, accompanied by enhanced particle integration, with higher molding pressures, similar to the LPS glass. However, at low molding pressures, they show fewer pores than the LPS glass because partial fracture occurs more effectively. Among them, Li_6PS_5Cl exhibits the fewest pores.

These observations are quantitatively confirmed in Fig. 3, showing the volume fraction and tortuosity of each sulfide SE as a function of molding pressure. These values were calculated from the X-ray CT images in Fig. 2 using a 3D image processing method. As shown in Fig. 3 (a), the volume fraction increases with the increasing molding pressure, owing to their room-temperature pressure sintering capability, reaching approximately 77 % at 200 MPa for all three sulfide SEs. However, at a low molding pressure of 15 MPa, the LPS glass exhibits a lower volume fraction than the other sulfide SEs, and Li_6PS_5Cl shows the highest volume fraction. In contrast, the tortuosity is highest in the LPS glass and lowest in Li_6PS_5Cl at 15 MPa, as shown in Fig. 3 (b). The tortuosity decreases with the increasing molding pressure, reaching approximately 1.2 at 200 MPa for all three sulfide SEs, resulting from particle integration. Therefore, the extent of the structural changes, namely the magnitudes of the changes in volume fraction and tortuosity with the increasing molding pressure, are more pronounced for the LPS glass, followed by LPS glass ceramic, and then Li_6PS_5Cl, which are considered fully amorphous, partially crystalline, and highly crystalline materials, respectively. This trend is attributed to the fact that, as shown in Fig. 2, the sulfide SEs are sufficiently sintered at high molding pressure, resulting in nearly the same volume fraction and tortuosity, whereas at low molding pressures, Li_6PS_5Cl undergoes more effective partial fracture and particle integration than the other sulfide SEs, leading to a higher volume fraction and lower tortuosity.

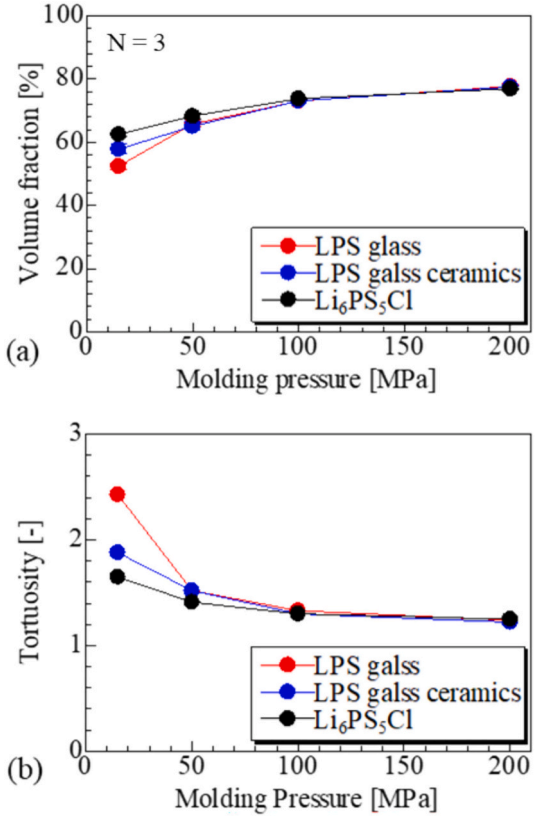

Fig. 3. Structural parameter changes of the sulfide SEs prepared using molding pressures of 15, 50, 100, and 200 MPa (N = 3, number of repeated measurements): (a) Volume fraction, (b) Tortuosity.

This difference in the microstructural changes can be further explained by considering the fracture toughness, which represents a material's resistance to particle breakage. Fig. 4 shows the fracture toughness of each sulfide SE, and Fig. 5 shows an illustration of the influence that fracture toughness has on the SE structure. According to Fig. 4, Li_6PS_5Cl has the lowest fracture toughness of 0.32 MPa·$m^{0.5}$, and LPS glass has the highest fracture toughness of 0.44 MPa·$m^{0.5}$. The lower fracture toughness of Li_6PS_5Cl may be attributed to the presence of grain boundaries within particles, facilitating crack initiation and propagation [39]. In contrast, the absence of grain boundaries in amorphous structures makes them less prone to fracture (i.e., less brittle). This suggests that the low fracture toughness of Li_6PS_5Cl promotes the onset of particle breakage at relatively low molding pressures, generating small particles that can effectively fill the pores between SE particles, as depicted in Fig. 5. In contrast, LPS glass has a higher fracture toughness and undergoes limited particle fracture, making pore filling and densification more difficult. As a result, the highly crystalline Li_6PS_5Cl exhibits a higher volume fraction and lower tortuosity at low molding pressures, whereas the fully amorphous LPS glass shows a lower volume fraction and higher tortuosity under the same low-pressure conditions. Consequently, the change in densification with the increasing molding pressure is most pronounced in LPS glass and least significant in Li_6PS_5Cl.

3.2. *Thermal transport characteristics of the sulfide SEs*

Fig. 6 (a) and (b) show the thermal conductivity and thermal diffusivity of each sulfide SE as a function of the molding pressure. The thermal conductivity was calculated based on the volume fraction shown in Fig. 3 (a) and the thermal diffusivity shown in Fig. 6 (b). The theoretical density and specific heat were determined from reference values [16]. Fig. 6 (c) shows the ionic conductivity of each sulfide SE as a function of the molding pressure. Fig. 6 (a) shows that the thermal conductivity significantly increases with the increasing molding pressure, yielding increases of approximately 2.3, 1.9, and 1.7 times for LPS glass, LPS glass ceramic, and Li_6PS_5Cl, respectively. In Fig. 6 (b), the thermal diffusivity slightly increases with the increasing molding pressure, increasing by approximately 1.5, 1.4, and 1.2 times for LPS glass,

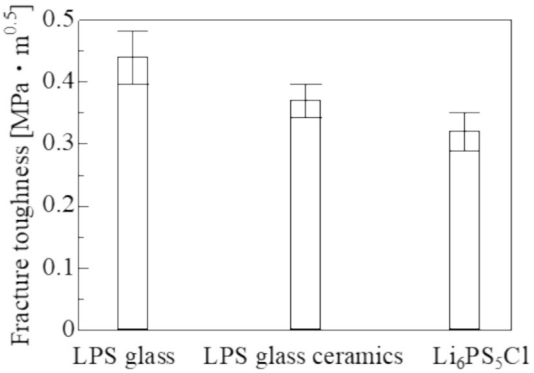

Fig. 4. Fracture toughness of the sulfide SEs prepared using a molding pressure of 200 MPa.

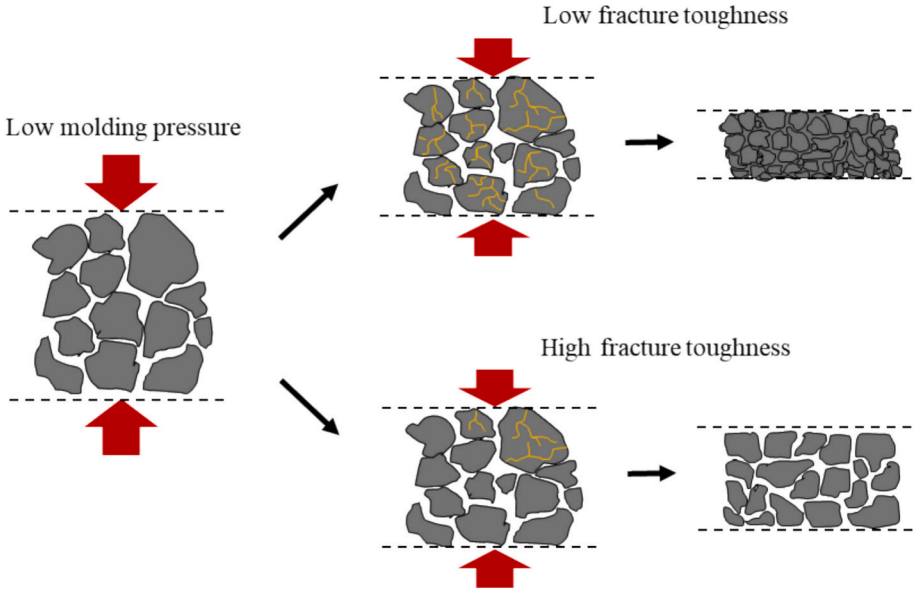

Fig. 5. Extent of the particle fracture and densification during room-temperature pressure sintering, depending on the fracture toughness of the material.

LPS glass ceramic, and Li_6PS_5Cl, respectively. These trends correspond with the extent of the increase in volume fraction and the decrease in tortuosity observed in Fig. 3, suggesting that the extent of the structural changes in the sulfide SEs correlates with the changes in thermal diffusivity and thermal conductivity. Fig. 6 (c) shows that the ionic conductivity significantly increases with the increasing molding pressure, and the argyrodite-type Li_6PS_5Cl exhibits higher ionic conductivity than LPS glass and LPS glass ceramic, as previously reported [17]. In the present study, the ionic conductivity increased by 2.7 times for Li_6PS_5Cl, 2.1 times for LPS glass ceramic, and 2.0 times for LPS glass, increasing more than the thermal diffusivity. This trend closely resembles the significant increase in thermal conductivity shown in Fig. 6 (a), suggesting that ion and heat transport exhibit analogous dependencies on the microstructural changes introduced during fabrication [17,40,41]. Heat conduction occurs not only through the SE but also through the pores; however, because the thermal conductivity of argon gas within the pores is significantly lower than that of the sulfide SEs, heat conduction is mainly facilitated by the solid phase. In addition, heat transfer via natural convection and radiation of the argon gas within the pores can be neglected because the temperature perturbation during thermal wave measurements is limited to ±1 °C and the pore size is sufficiently small. As the molding pressure increases, the volume fraction of the SE increases, providing more paths for heat conduction. This trend is consistent with the thermal conductivity behavior of porous Li_6PS_5Cl calculated using the Bruggeman model, as shown in Fig. S2. Simultaneously, the reduction in tortuosity mitigates the curvature of these paths, thereby enhancing thermal conductivity [40,41]. Ionic conductivity is also directly influenced by the volume fraction and tortuosity of the SE, although ions migrate exclusively through the SE rather than through the pores. Increasing the molding pressure leads to a higher SE volume fraction, facilitating the formation of more ion conduction paths. In addition, the accompanying decrease in tortuosity straightens these pathways, resulting in improved ionic conductivity [42]. Consequently, thermal conductivity and ionic conductivity increase as the volume fraction of the SE increases and its tortuosity decreases. Meanwhile, the increase in thermal diffusivity observed in Fig. 6 (b) is significantly smaller than the increases in thermal conductivity and ionic conductivity shown in Fig. 6 (a) and (c). This can be explained using Eqs. (6), (7), and (8) [25].

$$\alpha_p = k_p/\rho_p C_p \tag{6}$$

$$\rho_p = \rho_o \varepsilon \tag{7}$$

$$C_p = C_o \tag{8}$$

Here, α_p is the thermal diffusivity of porous material, k_p is the thermal conductivity of porous material, ρ_p is the corrected density of the porous material, ρ_o is the theoretical density, ε is the volume fraction of the porous material, C_p is the corrected specific heat of the porous material, C_o is the theoretical specific heat. The experimental raw data and literature values for each parameter are listed in Table S1. The increase in thermal diffusivity is attributed to the enhanced heat conduction paths and their reduced curvature, as shown in Eq. (6), but the accompanying increase in volumetric heat capacity ($\rho_p C_p$) suppresses these enhancements. This increase in $\rho_p C_p$ results from the rise in molding pressure, which increases the density of the porous material, as shown in Eq. (7). Thus, the higher density proportionally raises the volumetric heat capacity, leading to a relatively limited increase in thermal diffusivity compared with the increase in thermal conductivity.

3.3. Structural analysis of the oxide SEs

Fig. 7 shows cross-sectional SEM images of $Li_{6.25}Ga_{0.25}La_3Zr_2O_{12}$ prepared using different sintering temperatures, revealing the influence on microstructure. At 800 °C, a particulate structure was obtained, which became more integrated at 950 °C. This suggests that the particles were not sufficiently bonded at 800 °C, and their integration occurred at higher sintering temperatures (950 °C). At 1050 °C, the particulate structure was no longer visible, and new pores were generated. A reduction in both the number and size of pores (i.e., densification) was observed at 1100 and 1150 °C. In contrast to sulfide SEs, high-temperature sintering is required to achieve sufficient densification in the oxide SE [15,18,19]. The relatively high Young's modulus and strong ionic bonding between Li and O in oxide SEs significantly limit ion diffusion at particle boundaries [19].

Fig. 8 shows the volume fraction of $Li_{6.25}Ga_{0.25}La_3Zr_2O_{12}$ as a function of sintering temperature. The volume fraction was determined by calculating the ratio of the pellet density measured in this study to the theoretical density. As a result, the volume fraction increases with the increasing sintering temperature, sharply rising from approximately 57 % to 79 % in the 800 to 950 °C range. From 1050 to 1150 °C, the increase becomes more gradual, with the volume fraction reaching

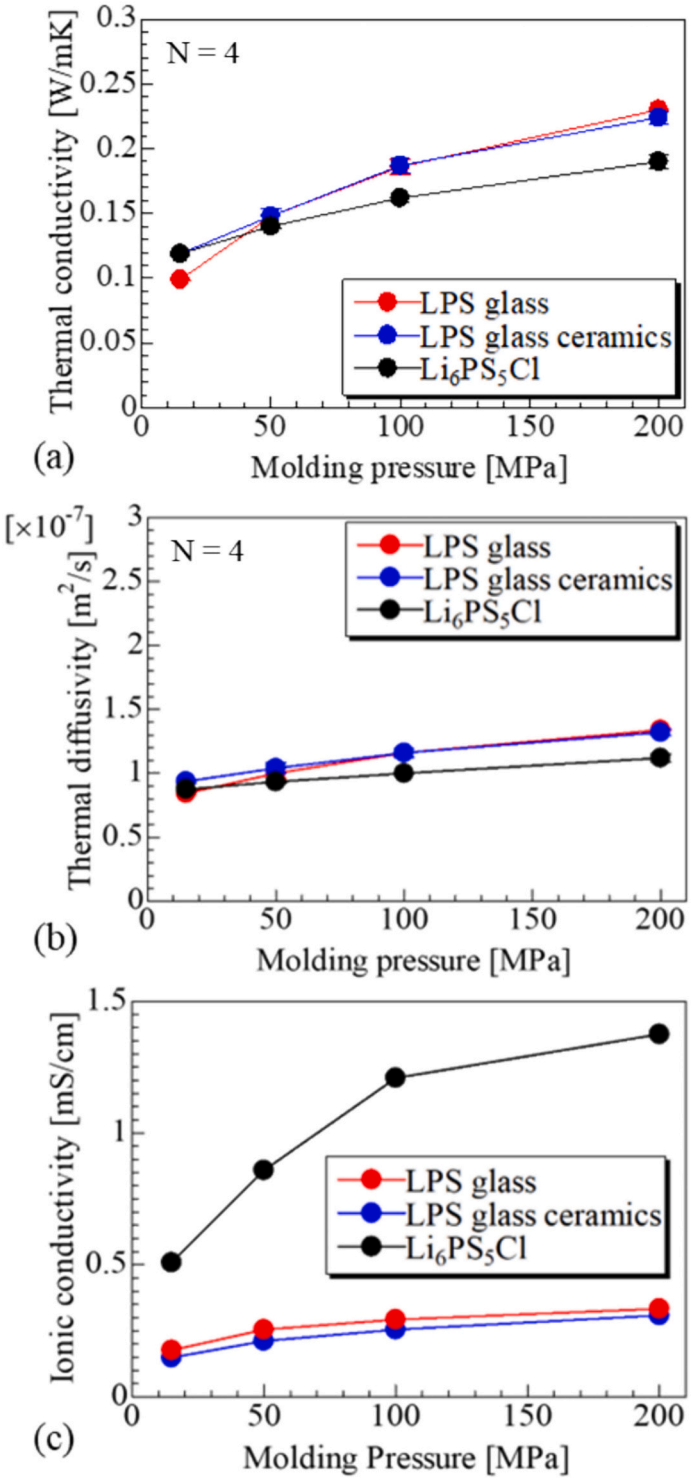

Fig. 6. Transport parameter changes of the sulfide SEs prepared using molding pressures of 15, 50, 100, and 200 MPa ($N = 4$, number of repeated measurements): (a) Thermal conductivity, (b) Thermal diffusivity, (c) Ionic conductivity.

approximately 86 % at 1150 °C. This indicates that the increase in sintering temperature has the most pronounced effect on the increase in volume fraction between 800 and 950 °C, during particle integration. Furthermore, a sintering temperature of at least 1050 °C is necessary to obtain densified $Li_{6.25}Ga_{0.25}La_3Zr_2O_{12}$, similar to the findings reported in previous work [18,19]. This is also consistent with the SEM observations shown in Fig. 7, where complete particle integration appears to occur above sintering temperatures of 950 °C. Shen et al. reported the study using high-resolution, nondestructive synchrotron X-ray tomography visualized the 3D microstructure of oxide SE and quantitatively demonstrated that the relative density increases with sintering temperature [18]. This result is consistent with the densification trend obtained in the present study, suggesting that the porosity and morphological changes identified through SEM observation and pellet density measurement appropriately reflect the microstructural evolution during sintering.

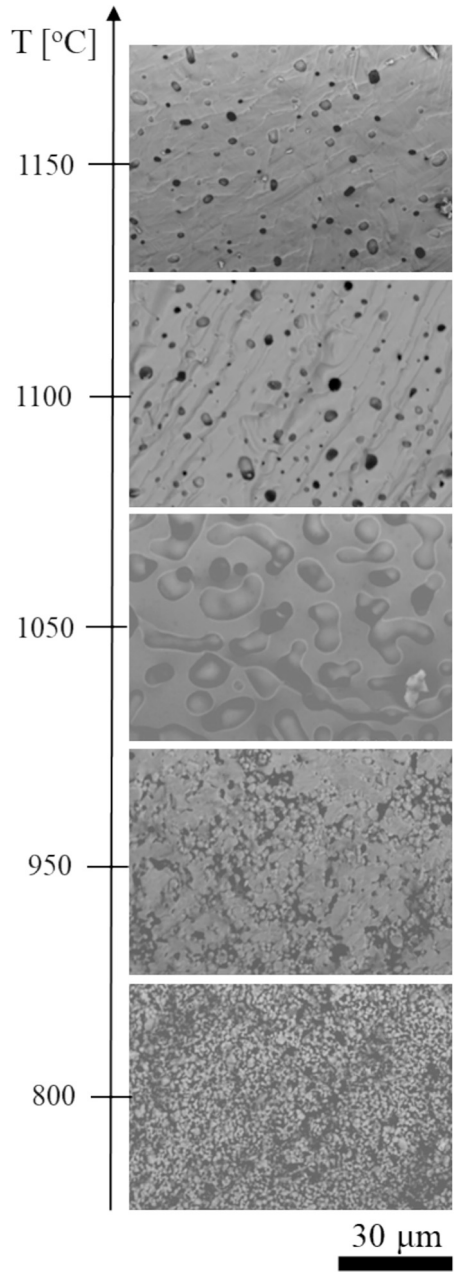

Fig. 7. Cross-sectional SEM images of $Li_{6.25}Ga_{0.25}La_3Zr_2O_{12}$ sintered at 800–1150 °C, microstructural evolution from particulate to densified structures with pore distribution (bright regions = $Li_{6.25}Ga_{0.25}La_3Zr_2O_{12}$, dark regions = pores).

3.4. Thermal transport characteristics of the oxide SEs

Fig. 9 (a) and (b) show the changes in the thermal conductivity and thermal diffusivity of $Li_{6.25}Ga_{0.25}La_3Zr_2O_{12}$ with the increase in sintering temperature. The thermal conductivity was calculated based on the volume fraction shown in Fig. 8 and the thermal diffusivity shown in Fig. 9 (b). The theoretical density and specific heat were determined from reference values [36,37]. Moreover, because the thermal conductivity of air trapped within the pores is significantly lower than that of the oxide SE, heat conduction predominantly occurs through the solid phase, and the contributions from natural convection and radiation within the pores are considered negligible. Notably, the thermal conductivity significantly increases with the increasing sintering temperature in Fig. 9 (a), suggesting that $Li_{6.25}Ga_{0.25}La_3Zr_2O_{12}$ behaves similarly to the sulfide SEs. Although high-temperature treatment is required for densification in the case of $Li_{6.25}Ga_{0.25}La_3Zr_2O_{12}$, which differs from sulfide SEs, an increase in the volume fraction promotes densification, which increases the number of heat conduction pathways and directly enhances thermal conductivity [15,25]. Meanwhile, in Fig. 9 (b), the thermal diffusivity slightly increases with the increasing sintering temperature. This is also similar to the behavior of the sulfide SEs. As shown in Eqs. (6), (7), and (8), the increase in thermal diffusivity is attributed to the thermal conductivity enhancement caused by densification. However, this effect is suppressed by a simultaneous increase in volumetric heat capacity. Therefore, the increase in thermal diffusivity resulting from densification at higher sintering temperatures is limited compared with the corresponding increase in thermal conductivity.

This study clarifies how densification during fabrication influences both thermal conductivity and thermal diffusivity of sulfide and oxide SEs. As sulfide SEs are known to decompose exothermically above 300 °C [43], enhanced thermal conductivity resulting from densification may help suppress the temperature rise required to trigger such reactions under abnormal conditions. However, the suppression of temperature rise cannot be regarded as resolved merely by an improvement in thermal conductivity. To mitigate such instabilities, it is essential to consider thermal diffusivity, which is explicitly used in the heat conduction equation to describe temperature gradients. Our results highlight that thermal diffusivity exhibits only a limited increase due to the effect of volumetric heat capacity even with densification. These findings provide novel insights by experimentally quantifying the impact of densification on thermal transport characteristics, which has rarely been demonstrated in previous studies. We note that the present work is limited to the material level and does not directly address cell-level thermal transport behavior. Nevertheless, the thermal transport properties characterized here serve as essential input parameters for future cell-level thermal simulations. While such modeling is beyond the scope of the present study, the findings provide foundational data for improving the thermal design and safety evaluation of ASSLiBs. As future work, we plan to extend this approach to electrode materials, investigating how fabrication parameters influence their thermal transport properties and incorporating these data into cell-level experiments and thermo-electrochemical simulations to evaluate heat generation and dissipation under realistic operating conditions.

4. Conclusions

ASSLiBs offer advantages such as improved safety and reduced cooling requirements, which contribute to an increase in the effective energy density. However, during high-rate charging and discharging, challenges related to degradation and non-uniform temperature distributions arise, adversely affecting battery performance. To address these challenges, we investigated the influence of microstructural changes in SEs during fabrication on their thermal conductivity and thermal diffusivity.

For the sulfide SEs studied herein, increasing the molding pressure enhanced particle integration and reduced the pore volume. This was accompanied by an increase in the volume fraction and a decrease in tortuosity, with noticeably larger variations in these parameters for LPS glass, followed by LPS glass ceramic and Li_6PS_5Cl. Additionally, owing to its low fracture toughness, Li_6PS_5Cl is more susceptible to particle fracture, resulting in a higher volume fraction and lower tortuosity than other sulfide SEs at low molding pressures. Regarding the thermal transport characteristics, the thermal conductivity increased more than the thermal diffusivity with the increasing molding pressure, corresponding with the structural changes and the variations in the volume fraction and tortuosity. The significant increase in thermal conductivity shows a similar trend to that of ionic conductivity, likely because the heat and ion transport have analogous characteristics. As the molding pressure increases, the volume fraction of the SE increases, providing more paths for conduction. Simultaneously, the reduction in tortuosity

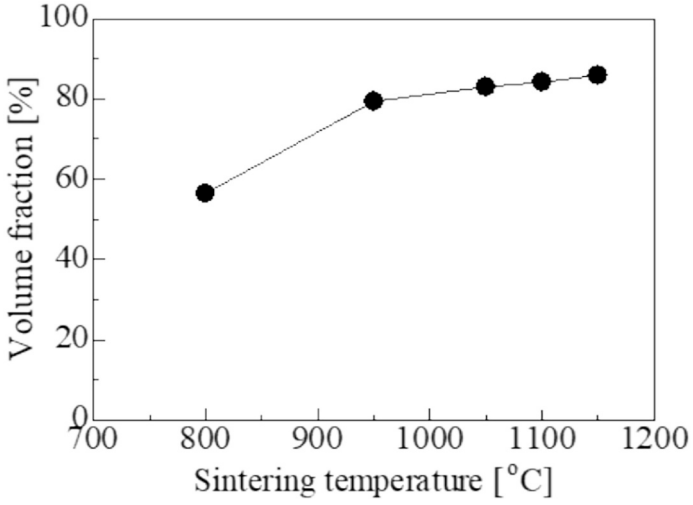

Fig. 8. Volume fraction changes of $Li_{6.25}Ga_{0.25}La_3Zr_2O_{12}$ prepared using sintering temperatures of 800–1150 °C.

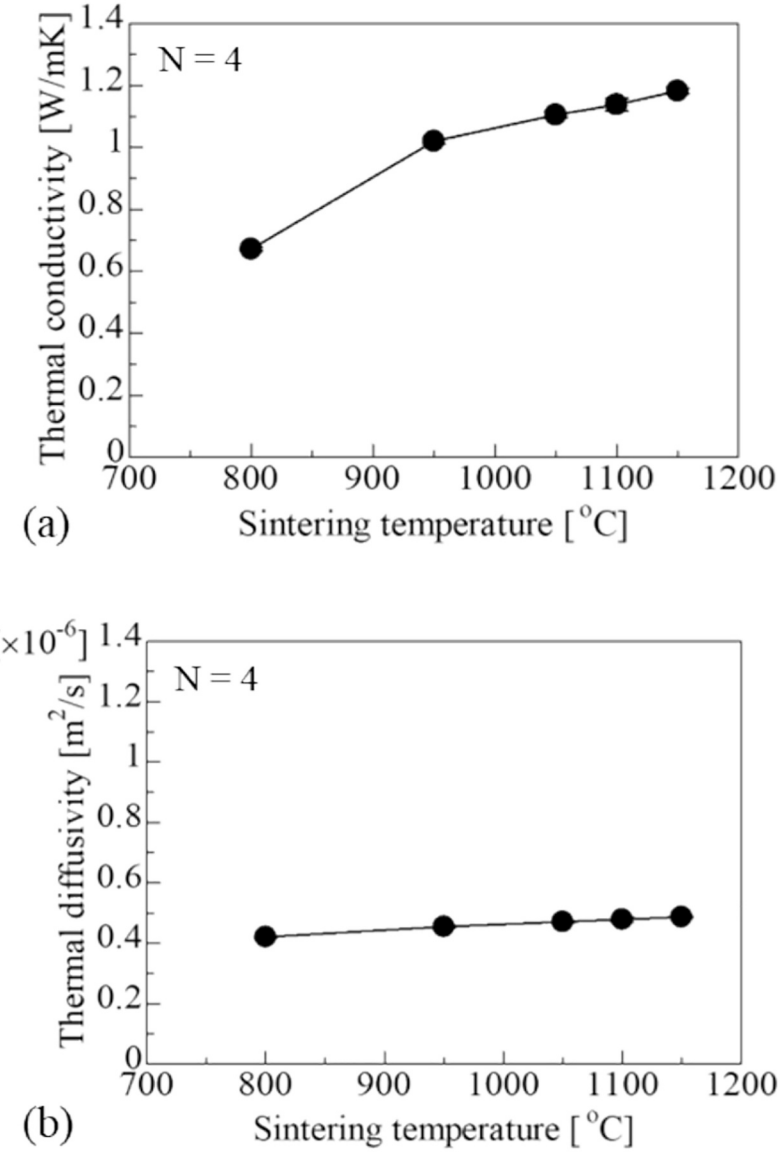

Fig. 9. Thermal transport changes of $Li_{6.25}Ga_{0.25}La_3Zr_2O_{12}$ prepared using sintering temperatures of 800–1150 °C (N = 4, number of repeated measurements): (a) Thermal conductivity, (b) Thermal diffusivity.

mitigates the curvature of these paths, thereby enhancing thermal and ionic conductivity. However, in the case of thermal diffusivity, the increase in thermal diffusivity due to the thermal conductivity enhancement resulting from the increased volume fraction and decreased tortuosity is suppressed by the accompanying increase in volumetric heat capacity due to structural densification.

For the oxide SE ($Li_{6.25}Ga_{0.25}La_3Zr_2O_{12}$), increasing the sintering temperature enhanced the particle integration and reduced the pore volume, ultimately increasing the volume fraction. Thermal diffusivity exhibited a slight increase at higher sintering temperatures, which is attributed to the increase in volumetric heat capacity due to structural densification, similar to that observed in the sulfide SEs.

Our study provides insight into the thermal transport behavior associated with structural changes in SEs and offers guidance for the optimization of SEs in high-performance ASSLiBs, while emphasizing the importance of considering not only thermal conductivity but also thermal diffusivity when discussing the thermal management of SEs.

CRediT authorship contribution statement

Hayoung Lee: Writing – original draft, Resources, Methodology, Investigation. **Yuto Seki:** Investigation. **Atsuro Okumura:** Investigation. **Manabu Kodama:** Writing – review & editing, Supervision, Software, Conceptualization.

Declaration of competing interest

The authors declare the following financial interests/personal relationships which may be considered as potential competing interests: Manabu Kodama reports financial support was provided by JKA foundation. Manabu Kodama reports financial support was provided by Japan Society for the Promotion of Science. If there are other authors, they declare that they have no known competing financial interests or personal relationships that could have appeared to influence the work reported in this paper.

Data availability

Data will be made available on request.

Acknowledgments

This study was partially supported by the Japan Keirin Autorace Foundation and JSPS KAKENHI Grant Number 22K17214.

Appendix A. Supplementary data

Supplementary data to this article can be found online at https://doi.org/10.1016/j.est.2025.119926.

References

[1] Y. Nishi, Lithium ion secondary batteries; past 10 years and the future, J. Power Sources 100 (2001) 101–106, https://doi.org/10.1016/S0378-7753(01)00887-4.
[2] T. Shan, P. Zhang, Z. Wang, X. Zhu, Insights into extreme thermal runaway scenarios of lithium-ion batteries fire and explosion: a critical review, J. Energy Storage 88 (2024) 111532, https://doi.org/10.1016/j.est.2024.111532.
[3] X. Feng, M. Ouyang, X. Liu, L. Lu, Y. Xia, X. He, Thermal runaway mechanism of lithium ion battery for electric vehicles: a review, Energy Storage Mater. 10 (2018) 246–267, https://doi.org/10.1016/j.ensm.2017.05.013.
[4] X. Yao, B. Huang, J. Yin, G. Peng, Z. Huang, C. Gao, D. Liu, X. Xu, All-solid-state lithium batteries with inorganic solid electrolytes: review of fundamental science, Chin. Phys. B 25 (2016) 018802, https://doi.org/10.1088/1674-1056/25/1/018802.
[5] B. Scrosati, J. Garche, Lithium batteries: status, prospects and future, J. Power Sources 195 (2010) 2419–2430, https://doi.org/10.1016/j.jpowsour.2009.11.048.
[6] C. Wu, J. Lou, J. Zhang, Z. Chen, A. Kakar, B. Emley, Q. Ai, H. Guo, Y. Liang, J. Lou, Y. Yao, Z. Fan, Current status and future directions of all-solid-state batteries with lithium metal anodes, sulfide electrolytes, and layered transition metal oxide cathodes, Nano Energy 87 (2021) 106081, https://doi.org/10.1016/j.nanoen.2021.106081.
[7] R. Chen, Q. Li, X. Yu, L. Chen, H. Li, Approaching practically accessible solid-state batteries: stability issues related to solid electrolytes and interfaces, Chem. Rev. 120 (2020) 6820–6877, https://doi.org/10.1021/acs.chemrev.9b00268.
[8] M. Gellert, E. Dashjav, D. Grüner, Q. Ma, F. Tietz, Compatibility study of oxide and olivine cathode materials with lithium aluminum titanium phosphate, Ionics 24 (2018) 1001–1006, https://doi.org/10.1007/s11581-017-2276-6.
[9] S. Larfaillou, D. Guy-Bouyssou, F. Le Cras, S. Franger, Comprehensive characterization of all-solid-state thin films commercial microbatteries by electrochemical impedance spectroscopy, J. Power Sources 319 (2016) 139–146, https://doi.org/10.1016/j.jpowsour.2016.04.057.
[10] R. Garcia-Mendez, F. Mizuno, R. Zhang, T.S. Arthur, J. Sakamoto, Effect of processing conditions of 75Li2S-25P2S5 solid electrolyte on its DC electrochemical behavior, Electrochim. Acta 237 (2017) 144–151, https://doi.org/10.1016/j.electacta.2017.03.200.
[11] Y. Kato, S. Hori, R. Kanno, Li_{10} GeP_2 S_{12} -type superionic conductors: Synthesis, structure, and ionic transportation, Adv. Energy Mater. 10 (2020) 2002153, https://doi.org/10.1002/aenm.202002153.
[12] T. Minami, A. Hayashi, M. Tatsumisago, Recent progress of glass and glass-ceramics as solid electrolytes for lithium secondary batteries, Solid State Ion. 177 (2006) 2715–2720, https://doi.org/10.1016/j.ssi.2006.07.017.
[13] S. Boulineau, M. Courty, J.-M. Tarascon, V. Viallet, Mechanochemical synthesis of Li-argyrodite Li6PS5X (X=Cl, Br, I) as sulfur-based solid electrolytes for all solid state batteries application, Solid State Ion. 221 (2012) 1–5, https://doi.org/10.1016/j.ssi.2012.06.008.
[14] R. Kanno, M. Murayama, Lithium ionic conductor thio-LISICON: The Li_2S-GeS_2-P_2S_5 system, J. Electrochem. Soc. 148 (2001) A742–A746, https://doi.org/10.1149/1.1379028.
[15] Y. Cui, M.M. Mahmoud, M. Rohde, C. Ziebert, H.J. Seifert, Thermal and ionic conductivity studies of lithium aluminum germanium phosphate solid-state electrolyte, Solid State Ion. 289 (2016) 125–132, https://doi.org/10.1016/j.ssi.2016.03.007.
[16] Z. Cheng, B. Zahiri, X. Ji, C. Chen, D. Chalise, P.V. Braun, D.G. Cahill, Good solid-state electrolytes have low, glass-like thermal conductivity, Small 17 (2021) 2101693, https://doi.org/10.1002/smll.202101693.
[17] M. Kodama, S. Komiyama, A. Ohashi, N. Horikawa, K. Kawamura, S. Hirai, High-pressure in situ X-ray computed tomography and numerical simulation of sulfide solid electrolyte, J. Power Sources 462 (2020) 228160, https://doi.org/10.1016/j.jpowsour.2020.228160.
[18] F. Shen, M.B. Dixit, X. Xiao, K.B. Hatzell, Effect of pore connectivity on Li dendrite propagation within LLZO electrolytes observed with synchrotron X-ray tomography, ACS Energy Lett. 3 (2018) 1056–1061, https://doi.org/10.1021/acsenergylett.8b00249.
[19] A. Sakuda, A. Hayashi, M. Tatsumisago, Sulfide solid electrolyte with favorable mechanical property for all-solid-state lithium battery, Sci. Rep. 3 (2013) 2261, https://doi.org/10.1038/srep02261.
[20] K.B. Kiradjiev, S.A. Halvorsen, R.A. Van Gorder, S.D. Howison, Maxwell-type models for the effective thermal conductivity of a porous material with radiative transfer in the voids, Int. J. Therm. Sci. 145 (2019) 106009, https://doi.org/10.1016/j.ijthermalsci.2019.106009.
[21] J. Ordonez-Miranda, J.J. Alvarado-Gil, Effect of the pore shape on the thermal conductivity of porous media, J. Mater. Sci. 47 (2012) 6733–6740, https://doi.org/10.1007/s10853-012-6616-7.
[22] C.Y. Zhao, Review on thermal transport in high porosity cellular metal foams with open cells, Int. J. Heat Mass Transfer 55 (2012) 3618–3632, https://doi.org/10.1016/j.ijheatmasstransfer.2012.03.017.
[23] L. Gong, Y. Wang, X. Cheng, R. Zhang, H. Zhang, Thermal conductivity of highly porous mullite materials, Int. J. Heat Mass Transfer 67 (2013) 253–259, https://doi.org/10.1016/j.ijheatmasstransfer.2013.08.008.
[24] H.-S. Choi, J.-H. Park, J.-H. Lee, The effect of porosity on the thermal conductivity of highly thermally conductive adhesives for advanced semiconductor packages, Polymers 15 (2023) 3083, https://doi.org/10.3390/polym15143083.
[25] J.F. Kerrisk, Thermal diffusivity of heterogeneous materials, J. Appl. Phys. 42 (1971) 267–271, https://doi.org/10.1063/1.1659581.
[26] C. Dietrich, D.A. Weber, S.J. Sedlmaier, S. Indris, S.P. Culver, D. Walter, J. Janek, W.G. Zeier, Lithium ion conductivity in Li_2 S–P_2 S_5 glasses – building units and local structure evolution during the crystallization of superionic conductors Li_3 PS_4, Li_7 P_3 S_{11} and Li_4 P_2 S_7, J. Mater. Chem. A 5 (2017) 18111–18119, https://doi.org/10.1039/C7TA06067J.
[27] A. Hayashi, S. Hama, T. Minami, M. Tatsumisago, Formation of superionic crystals from mechanically milled Li2S–P2S5 glasses, Electrochem. Commun. 5 (2003) 111–114, https://doi.org/10.1016/S1388-2481(02)00555-6.
[28] H. Deiseroth, S. Kong, H. Eckert, J. Vannahme, C. Reiner, T. Zaiß, M. Schlosser, Li_6 PS_5 X: a class of crystalline Li-rich solids with an unusually high Li^+ mobility, Angew. Chem. 120 (2008) 767–770, https://doi.org/10.1002/ange.200703900.
[29] J.-F. Wu, E.-Y. Chen, Y. Yu, L. Liu, Y. Wu, W.K. Pang, V.K. Peterson, X. Guo, Gallium-doped Li_7 La_3 Zr_2 O_{12} garnet-type electrolytes with high lithium-ion conductivity, ACS Appl. Mater. Interfaces 9 (2017) 1542–1552, https://doi.org/10.1021/acsami.6b13902.
[30] M. Kodama, K. Takashima, S. Hirai, Improvement of lithium-metal electrode performance of all-solid-state batteries by shot peening on solid-electrolyte surface, J. Power Sources 537 (2022) 231556, https://doi.org/10.1016/j.jpowsour.2022.231556.
[31] A. Ohashi, M. Kodama, N. Horikawa, S. Hirai, Effect of Young's modulus of active materials on ion transport through solid electrolyte in all-solid-state lithium-ion

battery, J. Power Sources 483 (2021) 229212, https://doi.org/10.1016/j.jpowsour.2020.229212.
[32] G.R. Anstis, P. Chantikul, B.R. Lawn, D.B. Marshall, A critical evaluation of indentation techniques for measuring fracture toughness: I, direct crack measurements, J. Am. Ceram. Soc. 64 (1981) 533–538, https://doi.org/10.1111/j.1151-2916.1981.tb10320.x.
[33] C.B. Ponton, R.D. Rawlings, Vickers indentation fracture toughness test part 2 application and critical evaluation of standardised indentation toughness equations, Mater. Sci. Technol. 5 (1989) 961–976, https://doi.org/10.1179/mst.1989.5.10.961.
[34] J. Morikawa, T. Kurihara, T. Hashimoto, G. Sherbelis, Thermal diffusivity of thermosetting materials by temperature-wave analysis, Thermochim. Acta 299 (1997) 95–100, https://doi.org/10.1016/S0040-6031(97)00141-X.
[35] T. Hashimoto, Y. Matsui, A. Hagiwara, A. Miyamoto, Thermal diffusivity measurement of polymer films by the temperature wave method using Joule-heating, Thermochim. Acta 163 (1990) 317–324, https://doi.org/10.1016/0040-6031(90)80413-S.
[36] G. Zhao, C. Luo, Q. Hua, Enhanced comprehensive performance of the LLZO series solid electrolyte via multifunctional additive, J. Eur. Ceram. Soc. 44 (2024) 2251–2260, https://doi.org/10.1016/j.jeurceramsoc.2023.11.045.
[37] E.A. Il'ina, A.A. Raskovalov, O.G. Reznitskikh, Thermodynamic properties of solid electrolyte Li7La3Zr2O12, J. Chem. Thermodyn. 128 (2019) 68–73, https://doi.org/10.1016/j.jct.2018.08.009.
[38] P. Perrenot, A. Fauchier-Magnan, M. Mirolo, L. Lecarme, P. Jouneau, A. Boulineau, P. Bayle-Guillemaud, C. Villevieille, Room-temperature sintering of amorphous thiophosphate solid electrolyte (Li_3PS_4): coupling morphological evolution to electrochemical properties, Adv. Funct. Mater. 34 (2024) 2310739, https://doi.org/10.1002/adfm.202310739.
[39] W. Xie, Z. Deng, Z. Liu, T. Famprikis, K.T. Butler, P. Canepa, Effects of grain boundaries and surfaces on electronic and mechanical properties of solid electrolytes, Adv. Energy Mater. 14 (2024) 2304230, https://doi.org/10.1002/aenm.202304230.
[40] D. Curran, J.M. Porter, A tomography-based effective thermal conductivity model for ceramic fiber insulation, Int. J. Heat Mass Transf. 160 (2020) 120224, https://doi.org/10.1016/j.ijheatmasstransfer.2020.120224.
[41] P.R. Shearing, N.P. Brandon, J. Gelb, R. Bradley, P.J. Withers, A.J. Marquis, S. Cooper, S.J. Harris, Multi length scale microstructural investigations of a commercially available Li-ion battery electrode, J. Electrochem. Soc. 159 (2012) A1023–A1027, https://doi.org/10.1149/2.053207jes.
[42] K. Otani, T. Muta, T. Furuta, T. Miyuki, T. Kaburagi, G. Inoue, Ionic conductivity prediction model for composite electrodes and quantification of ionic conductivity reduction factors in sulfide-based all-solid-state batteries, J. Energy Storage 58 (2023) 106279, https://doi.org/10.1016/j.est.2022.106279.
[43] X. Rui, D. Ren, X. Liu, X. Wang, K. Wang, Y. Lu, L. Li, P. Wang, G. Zhu, Y. Mao, X. Feng, L. Lu, H. Wang, M. Ouyang, Distinct thermal runaway mechanisms of sulfide-based all-solid-state batteries, Energ. Environ. Sci. 16 (2023) 3552–3563, https://doi.org/10.1039/D3EE00084B.